Glassy magnetic state and negative temperature coefficient of resistivity in $Mn_{3+\delta}In$

Snehashish Chatterjee, Prabir Dutta,* Saurav Giri, and Subham Majumdar†
School of Physical Sciences, Indian Association for the Cultivation of Science, 2A & B Raja S. C. Mullick Road, Jadavpur, Kolkata 700032, India

Surasree Sadhukhan and Sudipta Kanungo‡
School of Physical Sciences, Indian Institute of Technology Goa, Ponda 403401, Goa, India

Souvik Chatterjee
UGC-DAE Consortium for Scientific Research, Kolkata Centre, Sector III, LB-8, Salt Lake, Kolkata 700106, India

Manju Mishra Patidar,§ Gunadhor Singh Okram, and V. Ganesan
UGC-DAE Consortium for Scientific Research, University Campus, Khandwa Road, Indore 452017, India

(Received 27 April 2020; accepted 14 December 2020; published 31 December 2020)

The complex metallic alloy Mn_3In has recently attracted attention for being a probable candidate for the fully compensated half-metallic ferrimagnet. The compound is associated with a rather unusual negative coefficient of resistivity approximately above the ferrimagnetic, $T_C = 80$ K. Our investigation indicates that that the ground state of the alloy is spin-glass like, which possibly coexists with the ferrimagnetic state. The carrier density obtained from the Hall-effect measurement shows a jump below T_C; afterward, it gradually increases with lowering temperature and shows a saturating tendency at the lowest temperature. The electronic structure calculations indicate that, at the Fermi energy, dominant contributions come from minority-spin channels with larger bandwidth. In contrast, very weak but nonzero states arise from the majority-spin channel, and half metallicity can be ruled out. The calculations also found that the antiferromagnetic alignment of Mn spins with nonzero resultant magnetic moment confirms the ferrimagnetic nature consistent with the experimental results. The high-temperature phase with negative temperature coefficient of resistivity can be related to the localization of charge carriers through electron-phonon interactions.

DOI: 10.1103/PhysRevB.102.214443

I. INTRODUCTION

Mn-based intermetallic alloys have gained renewed attention due to their potential contribution in the field of shape memory alloys and spintronic applications [1,2]. The essence of spintronics applications is the half-metallic (HM) character of the materials, and the majority of the systems investigated so far are half-metallic ferromagnets (HMFs). HMFs possess a metallic channel for one spin and a semiconducting channel for the other spin, with complete spin polarization [3,4].

The presence of nonzero magnetic moment in HMF hinders the performance of spintronics devices. The problem can be overcome if we instead use a HM fully compensated ferrimagnet, which will produce a zero or very weak magnetic moment. Several transition-metal compounds such as MnCrSb and $Fe_8MnV_7Sb_7In$ are predicted to have such HM compensated ferrimagnetic character [5]. Recently, a different series of binary compounds with the general formula X_3Z (X = 3*d* transition metal and Z = *sp* element) has been investigated theoretically by Gao *et al.* [6] for HM ferrimagnetic character. Wurmehl *et al.* [7] concluded that, by the combination of the Slater-Pauling rule and the Kübler rule, a condition is obtained which predicts the binary Mn_3Z compounds to be the most practical candidates for attaining the HM-ferrimagnetic state.

Mn_3In belongs to the complex metallic alloy (CMA) group of compounds with cubic γ-brass structure (space group $P\bar{4}3m$) [8]. One unit cell of Mn_3In contains 52 atoms with two different atomic clusters each containing 26 atoms. On the other hand, each cluster of 26 atoms consists of four shells, viz. four atoms are present on the four vertices on the inner tetrahedron; four atoms are positioned on the outer tetrahedron; six atoms are on the vertices of the octahedra; and 12 atoms are placed on the cubooctahedron. Here cubooctahedron represents a polyhedron formed by joining the edges of the cube placed at the middle of octahedral faces. There can exist a significant mixture of Mn and In atoms on both octahedra and cubooctahedron sites in the 26 × 2-atom clusters of Mn_3In leading to antisite disorder [9,10].

Powder neutron diffraction and magnetic susceptibility studies by Brown *et al.* indicate Mn_3In to be a ferrimagnetic material below ≈75 K [11]. The neutron-diffraction indicates

*Present address: Jawaharlal Nehru Centre for Advanced Scientific Research, Jakkur, Bangalore, 560064, India.
†sspsm2@iacs.res.in
‡sudipta@iitgoa.ac.in
§Present address: Emerald Heights International School, A.B. Road, Rau, Indore, MP 453331, India.

only one magnetic propagation vector, which is denoted by $N/2$ for $N = 7$. Here $N = h^2 + k^2 + l^2$ with (hkl) being the Bragg reflection positions. Such an observation clearly indicates that the primary magnetic structure is collinear in nature. Very recently, Zhang *et al.* found a spin-glass-like (SG-like) ground state below 45 K [12]. The compound is also found to show a change in the sign of the temperature coefficient of resistivity upon cooling below about ferrimagnetic T_C. Despite theoretical predictions and experimental works, a comprehensive view of the electronic and magnetic properties for Mn_3In is still lacking, and there are few exquisite points that need to be addressed. First, it is rather unconventional to have a metallic ferrimagnetic (FiM) state being developed from a semiconducting paramagnetic (PM) state. Such a phase transition is quite the opposite to the regular Mott-Hubbard type of metal-insulator transition as the low-temperature antiferromagnetic (AFM) or FiM phase is supposed to be insulating (p. 887 of Ref. [13]). Second, the true electronic state of the material, i.e., whether Mn_3In is a HM-ferrimagnet or not as claimed by other groups [6,7], remains incomprehensible. Lastly, one also needs to identify the nature of the magnetic ground state of the material. Keeping these points in mind, we performed a joint experimental and theoretical investigation on Mn_3In, and our work indicates the system to be a quasi HM-FiM system with the signature of a magnetic glassy phase at low temperature.

II. EXPERIMENTAL DETAILS

A polycrystalline sample of Mn_3In was prepared by arc melting in an argon atmosphere. The as-cast ingot was vacuum-sealed in a quartz capsule and annealed at 800 °C for 15 h and quenched in ice water. The crystallographic structure was investigated by x-ray powder diffraction (XRD) and the Rietveld refinement was performed using the MAUD program [14]. Magnetic measurements were carried out by using a commercial Quantum Design SQUID magnetometer (MPMS XL Ever Cool model) as well as a vibrating sample magnetometer (Cryogenic Ltd., UK). The standard technique was used to measure electrical resistivity ($\rho = \rho_{xx}$) and Hall resistivity (ρ_{xy}) on a cryogen-free high-magnetic-field system (Cryogenic Ltd., U.K.) between 5 and 300 K. Thermopower measurements were performed in a laboratory-based setup using the standard differential technique in the temperature range 5–300 K. Heat-capacity measurements were performed on a Quantum Design Physical Properties Measurement System.

III. THEORETICAL DETAILS

Density-functional theory (DFT) based electronic structure calculations were performed using a plane-wave basis set based on a pseudopotential framework, as incorporated in the Vienna *ab initio* simulation package (VASP) [15,16]. The generalized gradient exchange-correlation approximated (GGA) functional was employed following the Perdew-Burke-Ernzerhof (PBE) prescription [17]. The missing onsite electron-electron correlation effect beyond GGA was taken into account through GGA + U calculations [18,19], where both $U = 5.9$ eV and $J_H = 0.9$ eV were applied. The plane-wave cutoff was employed to be 500 eV. A k-point mesh of $6 \times 6 \times 6$ in the Brillouin zone was used for self-consistent calculations. The internal positions of the atoms were relaxed toward equilibrium until the Hellmann-Feynman force becomes less than 0.001 eV Å^{-1} keeping the lattice parameters fixed at experimentally determined values.

IV. RESULTS

A. Powder x-ray diffraction

It has been found that a fully ordered Mn_3In seldom exists with proper 3 : 1 stoichiometry. The so-called ordered structure is off-stoichiometric and there can be primarily two different stoichiometries, namely, $Mn_{36}In_{16}$ (2.25 : 1 ratio of Mn and In) and $Mn_{40}In_{12}$ (3.33 : 1 ratio of Mn and In). On the other hand, there can exist a second structure ($Mn_{39}In_{13}$) with stoichiometric 3 : 1 ratio of Mn and In, albeit having random occupancy of Mn and In atoms (antisite disorder) [8]. Figure 1 depicts the powder XRD pattern of Mn_3In measured at room temperature, which confirms the sample to be a single phase. Rietveld refinement has been performed on the data considering both ordered [Figs. 1(a) and 1(b)] and disordered [Fig. 1(c)] structures. The atomic positions obtained from these refinements are shown in Table I. One can see from the table that there exists about 19% antisite disorder in the stoichiometric $Mn_{39}In_{13}$ structure. All the refinements fit the data quite well, and the calculated cubic lattice parameter is found to be 9.427(2), 9.429(8), and 9.428(7) Å, respectively for ordered [Figs. 1(a) and 1(b)] and disordered [Fig. 1(c)] structures, which are pretty close to the previously reported value [20]. The standard deviation σ_D of the x-ray refinements for the structures of Figs. 1(a)–1(c) are found to be 2.04, 2.07 and 1.89, respectively. However, such a small variation in σ_D may not be significant enough to identify the exact structure of the experimental sample. In our theoretical electronic structure calculations, we mostly used the $Mn_{40}In_{12}$ structure, which is nearly stoichiometric. In addition, the other ordered structure of $Mn_{36}In_{16}$ was also used for comparison. Since we cannot determine the Mn and In ratio exactly, it is therefore better to refer to the studied compound as $Mn_{3+\delta}In$ instead of Mn_3In.

B. Magnetization

The temperature T variation of magnetization (M/H) measured under an applied magnetic field of $H = 50$ Oe, 100 Oe, and 1 kOe in the zero-field-cooled (ZFC) and field-cooled (FC) conditions is presented in the main panel and upper inset of Fig. 2(a) [21]. $M(T)$ data are characterized by a broad hump-like feature around 100 K followed by a drop in M below 80 K upon cooling. This onset temperature for the drop in M has been assigned to a PM-to-FiM transition point ($T_C = 80$ K). The ZFC and FC curves bifurcate from each other slightly below T_C. The point of bifurcation is found to decrease with increasing magnetic field (89, 86, and 75 K, respectively, for $H = 50$, 100 Oe, and 1 kOe). The extent of bifurcation between FC and ZFC data also increases with decreasing values of H. Such behavior is often observed in disordered or glassy magnetic systems. The high-temperature (200–300 K) M/H data can be fit [see the inset of Fig. 2(a)]

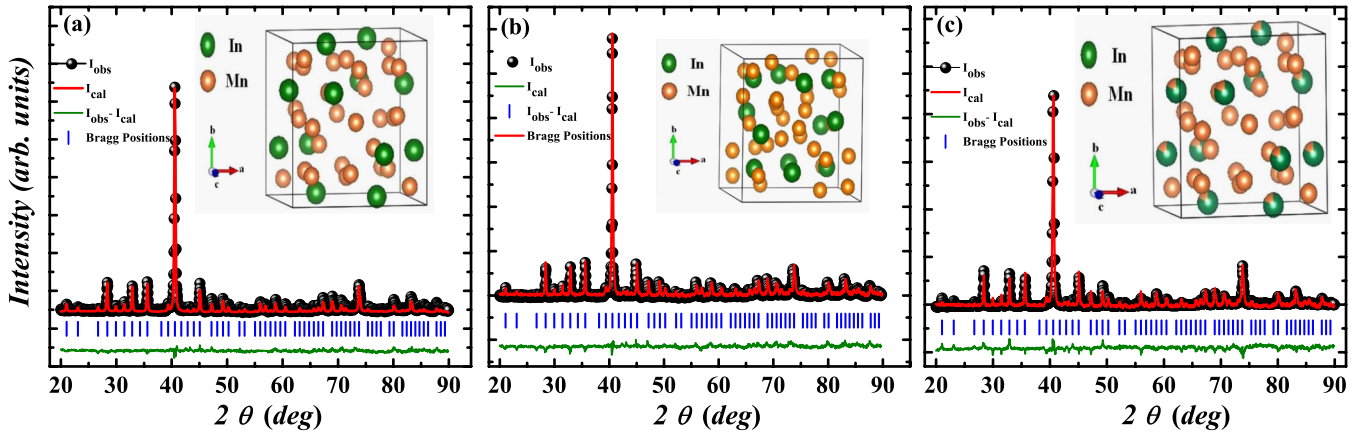

FIG. 1. XRD patterns of $Mn_{3+\delta}In$ (data points) at room temperature and the Rietveld refinement curves (solid line) for the three different crystallographic arrangements, namely, (a) ordered structure with Mn : In ratio 36 : 16, (b) ordered structure with Mn : In ratio 40 : 12, and (c) antisite disordered with 3 : 1 stoichiometry. The insets show the respective atomic arrangements.

with a modified Curie-Weiss law, $M/H = C/(T - \theta) + \chi_0$, where C is the Curie constant, θ is the PM Curie temperature, and χ_0 is the T-independent susceptibility. From the fitting, we obtain the paramagnetic moment, μ_{eff} to be $3.37\mu_B$/(f.u. of Mn_3In), and $\theta = 158$ K. The value of χ_0 is found to be small but positive. Despite the predicted FiM state, the observed positive value of θ indicates the presence of FM correlations in the system. In contrast with our data, the previous work [12] reported the value of θ to be around -200 K, and the estimated value of μ_{eff} from the published data is $4.4\mu_B$/(f.u. of Mn_3In). It is to be noted that the Curie-Weiss fit of the previous paper seems more convincing, as it was done over a much wider temperature range and away from the magnetic ordering temperature. The isothermal M vs H curves recorded at different constant temperatures ($T = 2, 5, 50, 100$, and 280 K), between -70 and 70 kOe, are plotted in Fig. 2(b). None of the isotherms saturates even at 70 kOe of field, and the hysteresis loop of the increasing and the decreasing legs

TABLE I. Atomic positions for possible ordered ($Mn_{36}In_{16}$), ($Mn_{40}In_{12}$) and disordered ($Mn_{39}In_{13}$) structures of $Mn_{3+\delta}In$ as obtained from the present refinement of the XRD data. Space group: $P\bar{4}3m$ (cubic).

	Sites	Atoms	Wyckoff positions	x	y	z	Occupancy
Ordered $Mn_{36}In_{16}$	In1	In	12i	0.320	0.320	0.0361	1.000
	In2	In	4e	0.6042	0.6042	0.6042	1.000
	Mn1	Mn	12i	0.196	0.196	0.540	1.000
	Mn2	Mn	6g	0.164	0.500	0.500	1.000
	Mn3	Mn	6f	0.360	0.000	0.000	1.000
	Mn4	Mn	4e	0.104	0.104	0.104	1.000
	Mn5	Mn	4e	0.328	0.328	0.328	1.000
	Mn6	Mn	4e	0.833	0.833	0.833	1.000
Ordered $Mn_{40}In_{12}$	In	In	12i	0.188	0.188	0.5451	1.000
	Mn1	Mn	12i	0.2895	0.2895	0.0532	1.000
	Mn2	Mn	4e	0.5982	0.5982	0.5982	1.000
	Mn3	Mn	6g	0.1487	0.500	0.500	1.000
	Mn4	Mn	6f	0.3415	0.000	0.000	1.000
	Mn5	Mn	4e	0.0948	0.0948	0.0948	1.000
	Mn6	Mn	4e	0.3353	0.3353	0.3353	1.000
	Mn6	Mn	4e	0.833	0.833	0.833	1.000
Disordered $Mn_{39}In_{13}$	In1	In(0.81) + Mn(0.19)	12i	0.310	0.310	0.037	1.000
	In2	In(0.81) + Mn(0.19)	4e	0.611	0.611	0.611	1.000
	Mn1	Mn	12i	0.208	0.208	0.567	1.000
	Mn2	Mn	6g	0.159	0.500	0.500	1.000
	Mn3	Mn	6f	0.360	0.000	0.000	1.000
	Mn4	Mn	4e	0.094	0.094	0.094	1.000
	Mn5	Mn	4e	0.333	0.333	0.333	1.000
	Mn6	Mn	4e	0.859	0.859	0.859	1.000

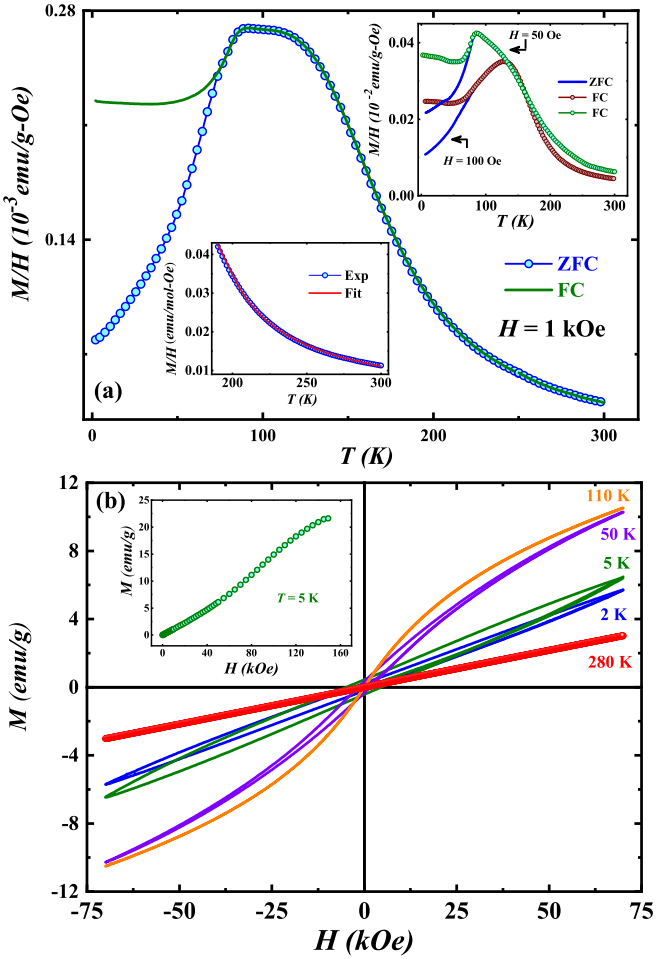

FIG. 2. (a) Magnetization (M/H) measured at 1 kOe as a function of temperature in ZFC and FC protocols. Upper inset shows M/H versus T measured at 50 Oe and 100 Oe as a function of temperature in ZFC and FC protocols. Lower inset shows modified Curie-Weiss fit to the magnetic susceptibility data. (b) Isothermal magnetization at different temperatures measured between ±70 kOe (five leg measurements including the virgin leg in the ZFC condition). Inset shows virgin M vs H isotherm measured up to 150 kOe of field in the ZFC state.

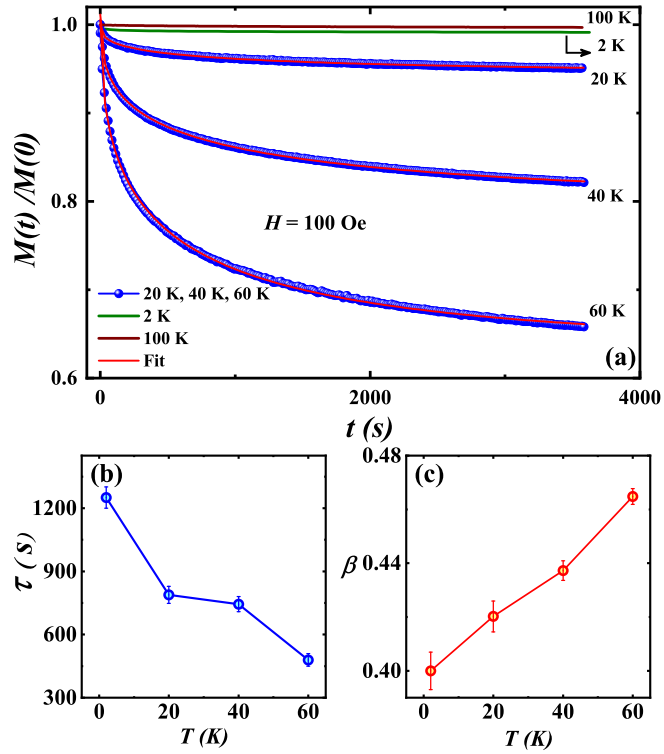

FIG. 3. (a) Time variation of M at different temperatures after the field is withdrawn. The solid lines are fits to the data with a stretched exponential function. (b), (c) Variation of fitting parameters τ and β, respectively, in the stretched exponential function.

do not join up even at the highest value of H. The value of the coercive field at 2 K is found to be about 2.7 kOe. The isotherm recorded at 50 and 100 K follow an "S-shaped" form with no saturation tendency at higher fields. The S-shaped form is absent in the isotherm recorded at 2 K. The absence of saturation of M at higher H rules out a ferromagnetic ground state of the system. The presence of finite coercivity also signifies that the sample is not AFM in nature. The other possibility with a collinear spin arrangement is FiM, which is better supported by the data. Interestingly, the values of M are found to be higher at 50 and 100 K than that of the 2 K one. This is consistent with the decreasing trend of M upon lowering of T in the M versus T data, and it further supports a FiM or AFM state. We also recorded M vs H data at 5 K up to $H = 150$ kOe of fields as shown in the top inset of Fig. 2(b). M does not saturate even at 150 kOe of field and the absolute value of M is quite small (≈22 emu/g or 1.1 μ_B/formula unit of Mn_3In) at the highest value of H.

C. Magnetic relaxation and memory

We measured magnetic relaxation at different temperatures ($T = 2$, 20, 40, 60, and 100 K) in the FC condition [Fig. 3(a)]. The sample was first cooled from 300 K to the desired temperature in the presence of $H = 100$ Oe and M was measured as a function of time t immediately after removing the field. The magnitude of relaxation is found to increase with increasing T. After $t = 1$ h, the sample shows about 35% change in M at 60 K, which is enormous as far as the relaxation in other glassy and disordered systems are concerned [22,23]. Upon further increase of temperature to $T = 100$ K, the relaxation drastically reduces because 100 K is above the magnetic transition temperature. This relaxation behavior can be fit with a modified stretched exponential (MSE) function given by $M(t) = M(0) + M_g \exp(\frac{-t}{\tau})^{\beta}$ [24,25]. Here $M(0)$ is the initial magnetization, M_g is the coefficient of the time-varying part, τ represents characteristic relaxation time, and β is the stretching exponent. The values of β and τ obtained from our fitting are shown in Figs. 3(b) and 3(c), respectively. The values of β are found to be within the limit 0.4 to 0.46 depending on the temperature of measurement. The value of τ increases with decreasing temperature, which is common below the spin freezing temperature of a glassy magnetic system [26]. The values of the parameters $M(0)$(emu/g) = 0.0121, 0.0096, 0.00786 and M_g(emu/g) = 0.000 686, 0.002 13, 0.001 75 as

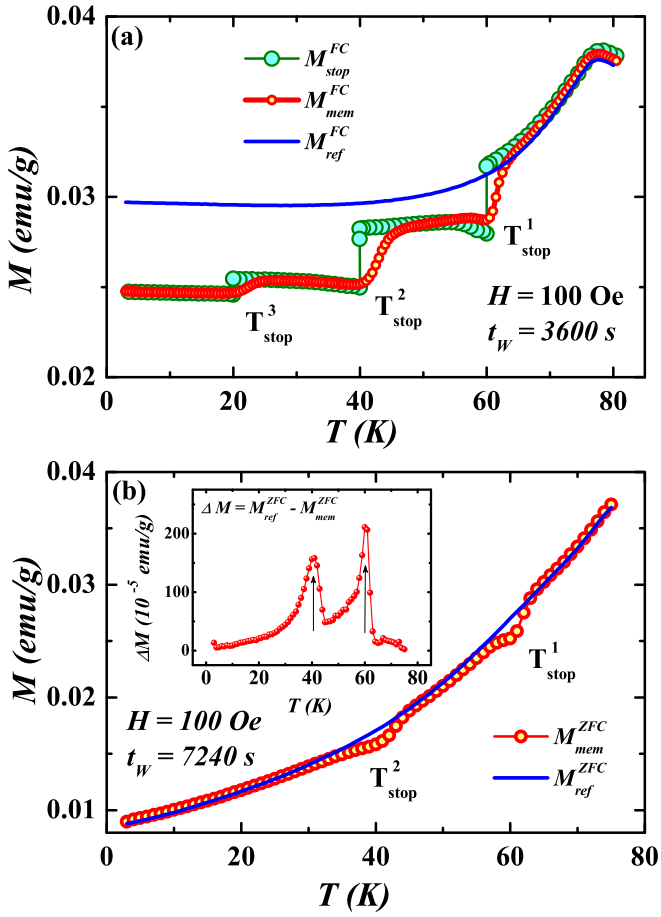

FIG. 4. (a) Field-cooled-field-stop memory curves (see text), and (b) zero-field-cooled memory curves. Inset of (b) shows ZFC difference curve.

obtained from the fitting of 20, 40, and 60 K relaxation data, respectively.

It is to be noted that the values of β and τ can be used to distinguish between a canonical (or atomic) spin glass and a cluster glass. In case of a cluster glass, FM or AFM spin clusters of assorted size can interact with each other. On the other hand a canonical glass has individual spins and/or infrequent and very tiny spin clusters that cause spin-freezing. It has been found that the values of β lies below 0.5 for canonical spin glasses [27–29]. In addition, τ shows an increasing trend with decreasing T, and the τ of our sample falls within the range for canonical CuMn spin-glass system [28].

The observed large relaxation following stretched exponential behavior is indicative of a glassy or disordered magnetic state. To examine the nature of the magnetic state, we performed field-cooled-field-stop memory measurements [see Fig. 4(a)] [30,31]. At first, the sample was cooled at $H = 100$ Oe from 300 to 2 K with intermediate stops at $T_{\rm stop} = 60$, 40, and 20 K of $t_w = 3600$ s each. The field was reduced to zero during $T_{\rm stop} = 60$, 40, and 20 K and reapplied after the waiting time $t_w = 3600$ s. This resulted in a step-like magnetization curve ($M^{\rm FC}_{\rm stop}$). After reaching 2 K, the sample was heated in the presence of $H = 100$ Oe without any stops ($M^{\rm FC}_{\rm mem}$). A reference curve is also presented in the same figure and was recorded in the FC protocol without any stops ($M^{\rm FC}_{\rm ref}$).

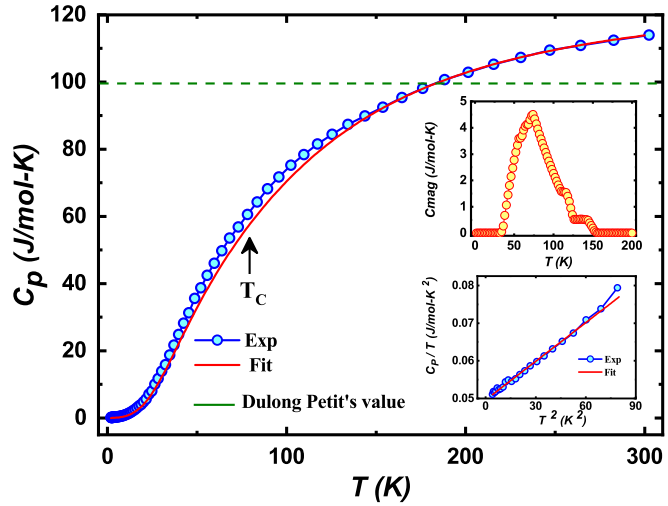

FIG. 5. Heat capacity (C_p) as a function of temperature. Inset (top): magnetic contribution to the heat capacity, inset(bottom): C_p/T versus T^2 data below 9 K.

The heating curve shows anomalies at the same temperatures where the sample was allowed to stop during cooling. This indicates the presence of FC memory in the system.

It is well known that superparamagnetic systems also show FC memory due to the anisotropy and distribution of relaxation time. To confirm the presence of an interacting glassy state, we measured memory in the ZFC condition [see Fig. 4(b)] [32]. The protocol is the same as that of FC memory except for the fact that no field is applied during cooling with stops. We found distinct features in the heating curve ($M^{\rm ZFC}_{\rm mem}$) at the stopping temperatures (60 and 40 K), pointing out the presence of ZFC memory. These features are clearer in the difference curve $\Delta M = M^{\rm ZFC}_{\rm mem} - M^{\rm ZFC}_{\rm ref}$ [inset of Fig. 4(b)]. The ZFC memory provides strong evidence in favor of an interacting magnetic glass, i.e., either cluster glass or canonical spin glass. However, looking at the strong signature of ZFC memory (it is clear even in the as-plotted heating data without the subtraction of the reference ZFC curve), the glassy state presumably represents a canonical one [33]. This is because the spin-flip time for the atomic spin glass is much shorter than bulky clusters in a cluster glass, which allows the canonical spin glass to access more metastable states in the energy landscape during the experiment [34].

D. Heat capacity

Figure 5 shows the T dependence of the heat capacity C_p measured in zero magnetic field. The high-temperature value exceeds the classical Dulong-Petit value of $3pR$ (=99.77 J mol^{-1} K^{-1}), where R is the gas constant and $p = 4$ is the number of atoms per formula unit. Such deviation from the classical value is very common, particularly in complex solids. We do not observe any well-defined peak in the $C_p(T)$ data around $T_C = 80$ K. We calculated the magnetic contribution ($C_{\rm mag}$) to the heat capacity by subtracting the nonmagnetic part (C_{nm}) from $C_p(T)$ [35]. $C_{nm}(T)$ is obtained by fitting $C_p(T)$ data with a Debye-Einstein law between 150 and 300 K and subsequent extrapolation to low temperatures

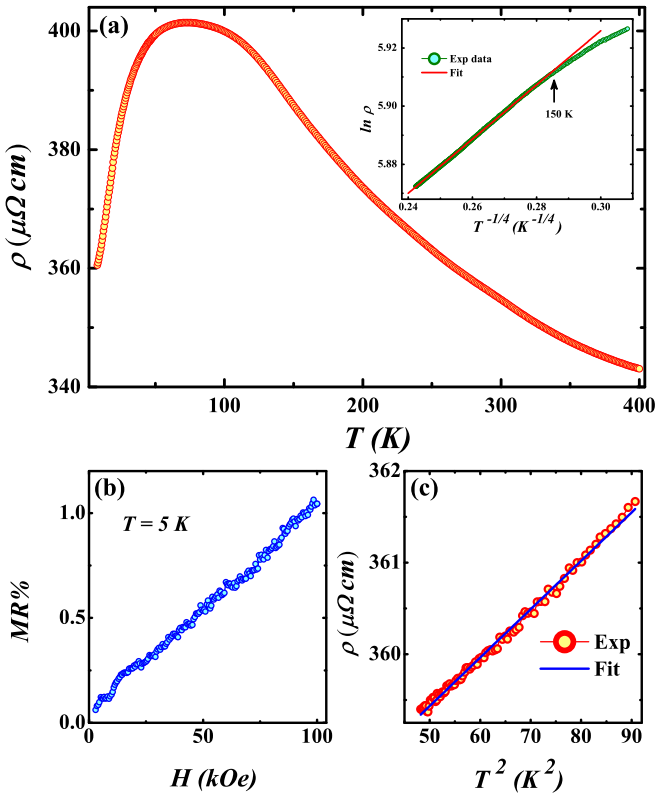

FIG. 6. (a) Electrical resistivity as a function of temperature. Inset of panel (a) shows fitting of high temperature resistivity data with variable range hopping model. (b) Magnetoresistance as a function of field measured at 5 K. (c) Low-temperature resistivity (ρ) plotted as a function of T^2.

[36]. Clearly, $C_{\rm mag}(T)$ shows a broad peak centered around $T_C = 80$ K. The broadness of the peak is likely to be connected with the glassy magnetic phase [37,38], as is evident from the relaxation and memory experiments.

The $C_p(T)/T$ versus T^2 data show linear behavior between 2 and 8 K (bottom inset of Fig. 5) implying a $\gamma_e T + \beta_l T^3$ type variation of total C_p at low temperatures. For an ordinary metal, $\gamma_e T$ and $\beta_l T^3$ are, respectively, the electronic and lattice contributions to the heat capacity. From the linear fit to the data below 8 K, we obtain $\gamma_e = 49.4$ mJ mol^{-1} K^{-2} and $\beta_l = 0.34$ mJ mol^{-1} K^{-4}. In the heat-capacity data, the molecular weight is calculated concerning the chemical formula Mn_3In.

E. Electrical resistivity

The T variation of ρ in $Mn_{3+\delta}In$ in the absence of H is represented in Fig. 6(a). It shows a negative temperature coefficient of resistivity ($d\rho/dT < 0$) down to about 80 K, followed by a well-defined metallic state ($d\rho/dT > 0$) upon further lowering of T. This behavior matches quite well the previous transport data [12]. The T variation of conductivity of $Mn_{3+\delta}In$ above about 80 K (where $d\rho/dT < 0$) cannot be fit with a simple activated-type behavior. A negative resistivity coefficient is rather uncommon among intermetallic alloys and compounds. For example, Mn_2CoAl with FiM ground state shows semiconducting behavior down to 2 K [39] without a change in the sign of $d\rho/dT$. It is to be noted that the magnitude of ρ in $Mn_{3+\delta}In$ is fairly low even in the high-temperature phase ($\rho \approx 350$ $\mu\Omega$ cm at 300 K) [40]. Considering the presence of antisite disorder in the system, we have fit the $\rho(T)$ of the high-temperature state with a Mott variable range hopping (VRH) type model, $\rho(T) = \rho_1 \exp(T_0/T)^{1/4}$ [41], where ρ_1 and T_0 are constants. A good fitting is only observed between 150 to 290 K, which indicates that localization due to disorder has some role in the semiconducting phase [see inset of Fig. 6(a)].

We carried out isothermal H variation of ρ at different constant T, and a small change in ρ is seen under the application of H. At 5 K, the magnetoresistance [MR $= [\rho(H) - \rho(0)]/\rho(0)$] is found to be positive with a magnitude around 1% for $H = 100$ kOe [see inset of Fig. 6(a)]. Interestingly, this positive MR shows a linear field dependence, which might be connected with the inherent disorder present in the sample [42].

We carefully examined the low-temperature part of the zero-field resistivity data [Fig. 6(c)] and found that below about 10 K, ρ follows a quadratic T dependence, $\rho(T) = \rho_0 + AT^2$, where ρ_0 is the residual resistivity. The value of the coefficient A turns out to be 5.2×10^{-8} Ω cm K^{-2}, which is significantly large compared with common metals such as Cu [43–45]. The value of γ_e, as obtained from our low-temperature $C_p(T)$ data, is also moderately large (49.4 mJ mol^{-1} K^{-2}). For heavy-fermion (HF) systems with enhanced values of A and γ_e, the Kadowaki–Woods scaling law [46] is often found to be valid: $A/\gamma_e^2 \sim 1 \times 10^{-5}$ $\mu\Omega$ cm mJ^{-2} mol^2 K^2. Here A/γ_e^2 is found to be 2.2×10^{-5} $\mu\Omega$ cm mJ^{-2} mol^2 K^2, which is quite close to the expected scaling behavior. The observed deviation from unity of the ratio is not unusual and is observed in many FM and nearly FM transition metals [47].

F. Hall and thermopower measurements

We measured the Hall resistivity (ρ_{xy}) at different constant temperatures, and the variation of ρ_{xy} with H is depicted in Fig. 7(a) [48]. Note that, up to $H = 40$ kOe, ρ_{xy} shows an almost linear variation with H between 10 and 300 K. ρ_{xy} is negative at all temperatures, indicating that electrons are the majority carriers in the system. We have calculated the charge-carrier density n_H from the Hall data (Table II), and it is plotted in Fig. 7(b). Despite the sample being magnetic, there is no significant signature of the anomalous Hall effect (AHE) in our measurement, which is generally observed in the low-field regime. To avoid any contribution from AHE towards n_H, we have used ρ_{xy} data in the high-field region (20–40 kOe) for the calculation. The extrapolation of the linear ρ_{xy} vs H plot between 20 and 40 kOe on the vertical axis gives us the maximum value of AHE, $\rho_{\rm AHE} \approx 0.06$ $\mu\Omega$ cm, which is about two orders of magnitude lower than the ordinary Hall effect observed in the sample. Such a small value of $\rho_{\rm AHE}$ can be due to the small resultant magnetic moment of the system [49,50].

A strong T variation of the calculated n_H is evident from the plot. n_H is almost constant above 100 K, and it shows a strong upturn upon cooling below 100 K. This corresponds to the change in the sign of $d\rho/dT$ observed around T_C in the

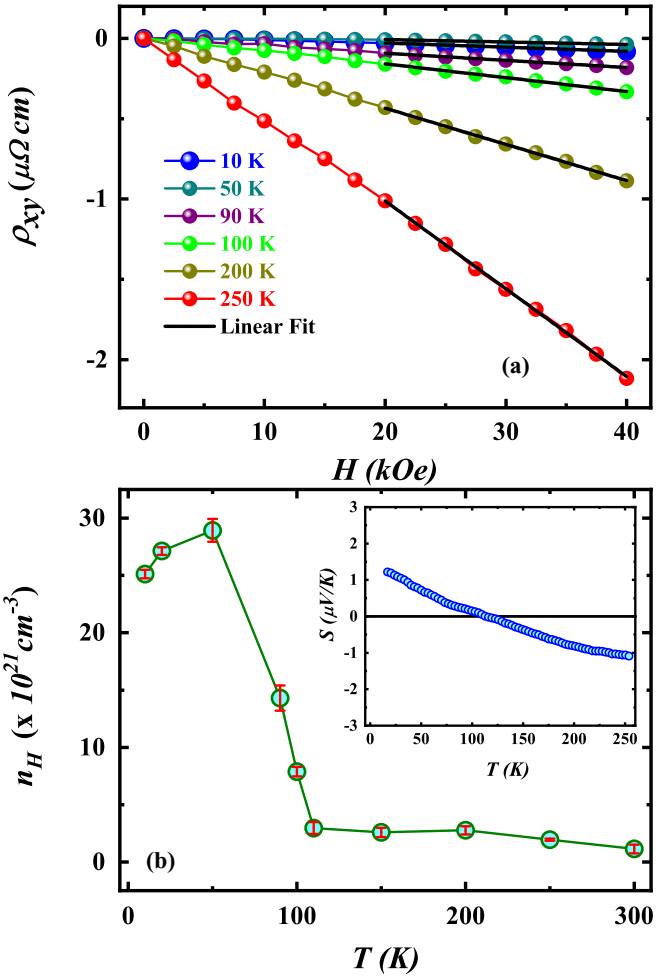

FIG. 7. (a) Variation of Hall resistivity ρ_{xy} as a function of magnetic field at different temperatures. (b) Carrier density n_H as obtained from the Hall-effect measurement as a function of temperature. Inset shows temperature variation of Seebeck coefficient S.

$\rho(T)$ data. The value of n_H is 2.4×10^{22} cm^{-3} at 10 K, which is expected for a metallic state. n_H tends to saturate at low temperature. At room temperature, n_H is about two orders of magnitude less [51].

To clarify the change in sign of $d\rho/dT$ in $Mn_{3+\delta}In$, we measured the T dependence of the Seebeck coefficient (S) [52] [see inset of Fig. 7(b)]. The value of S is found to be small over the entire temperature range between 10 and 250 K (varies between 1 and -1 μV/K), showing the highly metallic nature of the material consistent with the resistivity data [Fig. 6(a)]. For example, the thermopower of Mn_3Sn (tetragonal) and Mn_2CoSn (full Heusler structure), with similar values of resistivity, show one order of magnitude higher values of S [39] than the presently observed values. Below 100 K, S is positive, while it turns negative at higher temperatures. Notably, the sign change in S occurs around the magnetic ordering as well as the temperature where $d\rho/dT$ changes sign. In the simple Drude-Sommerfeld model, the thermopower can be expressed as

$$S(T) = \frac{8\pi^2 k_B^2 T}{3eh^2} m^* \left(\frac{\pi}{3n}\right)^{2/3} = \frac{\pi^2 k_B^2 T}{3eE_F}, \qquad (1)$$

TABLE II. Ordinary Hall coefficient ($R_O = \rho_{xy}/H$), carrier concentration n_H, and carrier mobility μ_H at different temperatures as obtained from our experimental data. For the ordinary Hall effect, we have used the ρ_{xy} data between 20 and 40 kOe.

T (K)	R_O (10^{-9} m^3/C)	$n_H = 1/(R_O e)$ (10^{21} cm^{-3})	$\mu_H = R_O/\rho_{xx}$ (cm^2 V^{-1} s^{-1})
10	−0.26	24.1	0.71
50	−0.22	30.1	0.38
100	−0.78	8.0	2.0
250	−3.0	2.1	9.0
300	−4.8	1.3	15.1

where E_F is the Fermi energy, e is the charge of the carriers (electron or hole), n is the density of carriers, m^* is the effective mass, and k_B is the Boltzmann constant [53]. Naively, the change in sign of S may indicate a change in carrier type (from electron to hole). In the case of correlated electron systems such as $Mn_{3+\delta}In$, one should be careful in using such a simple model to ascertain the nature of the charge carrier, because of (i) its off-stoichiometric nature, (ii) possible random occupancy of Mn and In atoms (antisite disorder), and (iii) prevalence of some excess Mn in the system. One can notice that S does not show a linear T dependence as in the Drude-Sommerfeld model. In addition, unlike thermopower, the Hall coefficient does not change sign below 100 K.

G. Theoretical calculations

The spin-polarized GGA + U ($U_{\text{eff}} = 5$ eV) density of states (DOS) is shown in Fig. 8. The calculated magnetic moments at the Mn sites are $4.2\mu_B$. Although In is nonmagnetic, it gains a substantial induced moment ($\approx 0.3\mu_B$) and remains antiparallel to the Mn moment. The electronic structure

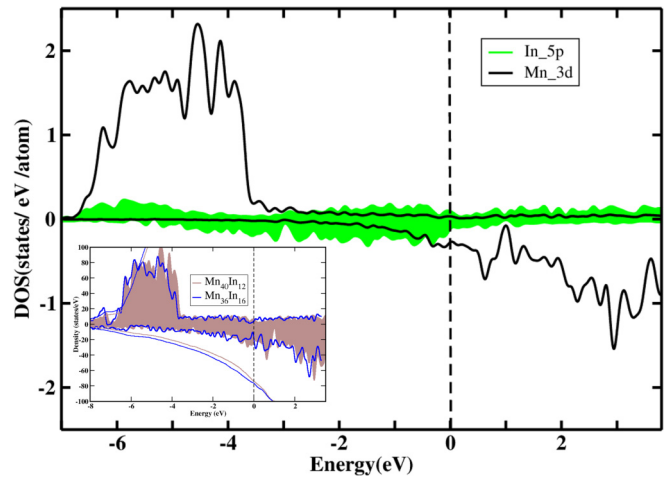

FIG. 8. Orbital-projected spin-polarized GGA + U DOS for $Mn_{40}In_{12}$. The dark and light lines represent Mn $3d$ and In $5p$ states, respectively. The two panels represent the majority- and minority-spin channels, respectively. Inset compares total DOS between the two phases, viz. $Mn_{36}In_{16}$ (dark blue line) and $Mn_{40}In_{12}$ (light brown shade), along with the integrated DOS by the dotted lines in the inset. The Fermi level is set at zero in the energy scale.

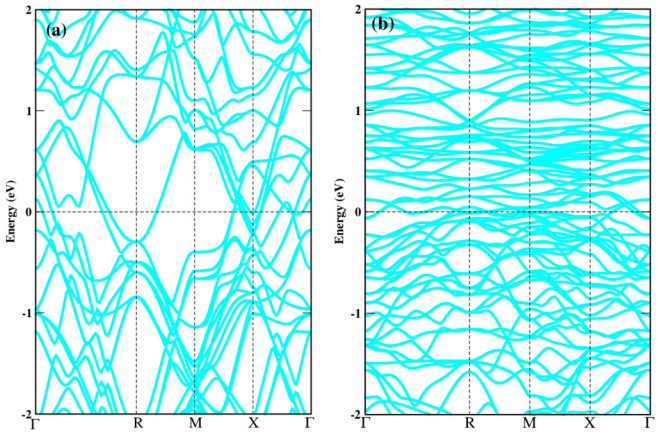

FIG. 9. Spin-polarized GGA $+U$ ($U_{\text{eff}} = 5$ eV) band structure for $Mn_{40}In_{12}$ along the high symmetry directions of the Brillouin zone. (a) and (b) represent total band structures for majority and minority spin channels, respectively. The Fermi level set at zero in the energy scale.

indicates that there is a finite DOS at the Fermi level E_F [54] without any gap both in the majority- and minority-spin channels. However, at E_F, the dominant contribution comes from the minority-spin channel, while the majority-spin channel shows very small DOS. The orbital projected and integrated DOS shows that the Mn $3d$ states in the majority-spin channel are almost filled and the minority-spin channel makes a substantial contribution at E_F. Notably, the contribution from the In $5p$ states are very small in the entire energy range. We have cross-checked the calculated electronic structure over the range of $U_{\text{eff}} = 4$ to 6 eV values that are usually used for calculations [55–58] and found that there are no such drastic changes in the main features of the electronic structure except the expected increase in the magnetic moment ($4.1\mu_B$, $4.2\mu_B$, and $4.3\mu_B$ for $U_{\text{eff}} = 4$, 5, and 6 eV, respectively) at the Mn sites due to the majority-spin channel Mn states are pushed up in energy scales, while the states in the minority-spin channel are least affected by changing the U values, as shown in Fig. A of the Supplemental Material [59].

Figure 9 presents an enlarged view of the band structure around E_F. It indicates that only a few bands cross the Fermi energy in the majority-spin channel compared with that of the minority-spin channel, which is also restricted in the given region of the Brillouin zone (BZ). At the center of the BZ, near the Γ point, the majority bands are more dispersive compared with the other regions in momentum space. However, many bands in the minority-spin channel from the Mn $3d$ lies on E_F and make it more metallic. It is evident that the intermetallic compound under investigation does not fall under the conventional HM state, where one spin channel is completely gapped and electrons conduct through the other spin channel only. Although primarily conducting through the minority-spin channel, there are very small but finite states from the majority-spin channel at E_F.

We have also compared the DOS of two ordered structures, namely, $Mn_{40}In_{12}$ and $Mn_{36}In_{16}$. We do not observe any significant difference in DOS of these two configurations, as reflected in the total density of states plot in the inset of Fig. 8, where $Mn_{40}In_{12}$ (nearly stoichiometric, Mn excess) and $Mn_{36}In_{16}$ (off-stoichiometric, Mn deficit) show a similar DOS at E_F.

As already mentioned, Mn_3In γ brass alloy is prone to antisite disorder. It is, therefore, important to know the effect of disorder on the electronic structure of the material. Experimentally, it is always difficult to identify the exact site occupancy of Mn and In in the presence of antisite disorder. Therefore, we have investigated the disordered structure theoretically by taking into consideration different atomic site arrangements that keep the number of respective atoms the same as that of the ordered $Mn_{40}In_{12}$. Since it is not possible to handle a completely disordered structure through the density-functional theory (DFT) type of *ab initio* method, which is based on Bloch periodicity, we took the ordered structure and on top of that and introduced disorder by interchanging the Mn and In sites. In every disordered configuration, we have exchanged different Mn sites with different In sites. In principle, there can be a huge number of possible disordered configurations, however, by the symmetry argument, we have done comparative investigation among the few representative disordered configurations, as shown in figure B of the Supplemental Material [59]. We did structural optimizations in each disordered configurations by relaxing the Mn and In atomic up to a cutoff force of 0.005 eV Å^{-1}, keeping the lattice parameters the same as that obtained from the experiments. The comparison of the calculated total DOS for the different disordered Mn-In configurations is shown in Fig. C of the Supplemental Material [59]. It shows that there are no such changes in the DOS among the different disordered configurations. Although at the Fermi energy, the minority-spin channel DOS differ slightly from each other (the enlarged view in the top inset), the basic nature as well as the integrated DOS remain exactly similar (as shown in the bottom inset of Fig. C). Also, the total-energy calculations among the different disordered configurations point out that the experimentally determined Mn-In site arrangement (on which structure we did all the calculations in the main paper) is energetically lowest by around 5 meV. Therefore, the conclusions drawn here are robust with respect to the Mn-In antisite disordered nature.

Since $Mn_{3+\delta}In$ has been found to show FiM-type behavior experimentally, it is worth investigating the magnetic interactions of this material through the DFT total-energy calculations. The result of the total-energy calculations for the $Mn_{40}In_{12}$ unit cell for different spin configurations is tabulated in Table III. More elaborative results are presented in Table A of the Supplemental Material [59]. In principle, $^{40}C_2$ spin configurations are possible for the unit cell containing 40 Mn sites. However, such huge numbers of self-consistent calculations are difficult to handle, so we used physical argumentation to reduce the spin configurations. In the $Mn_{40}In_{12}$ crystal structure, if we consider only the Mn sublattice, there are in total six structural units, as clearly shown in Fig. 10, viz. octahedral units (yellow bonds), two inner tetrahedral units (orange and blue bonds), two outer tetrahedral units (gray and green bonds), and cubooctahedron (red bonds). We choose few spin configurations to make fully compensated moments with equal numbers of up and down spins and other way we consider the spin configurations by assigning

TABLE III. Comparison of calculated (GGA + U with $U_{\text{eff}} = 5$ eV) total-energy differences ΔE for the lowest five energy spin configurations for $Mn_{40}In_{12}$ containing 40 Mn sites in the cell (Fig. 10). ΔE are calculated with respect to the lowest-energy configuration (i.e., AFM19). A more detailed spin configuration is given in Table A of the Supplemental Material [59].

Configuration	Spin arrangements	ΔE (meV/f.u.)	Resultant magnetic moment (μ_B/f.u.)
AFM5	15× ↑ 15× ↓ 10× ↑	48.69	0.14
AFM19 (OT-big antiparallel)	24× ↑ 4× ↓ 12× ↑	0	10.03
AFM27	24× ↑ 4× ↓ 12× ↑	64.18	7.76
AFM28	12× ↑ 16× ↓ 12× ↑	52.34	0.00
AFM29	12× ↑ 12× ↓ 4× ↑ 4× ↓ 4× ↑ 4× ↓	59.25	0.08

them in the structural unit wise. The few energetically lowest spin configurations are shown in Fig. D of the Supplemental Material [59]. The calculations show that in the energetically lowest configurations, the outer tetrahedron Mn unit (as shown by the green bonds in the Fig. 10) is antiferromagnetically aligned with respect to the other structural units with resultant magnetic moments of $\approx 10.03 \mu_B$/(f.u. of $Mn_{40}In_{12}$ unit cell). This confirms the FiM nature and corroborates the experimental data. The energy differences between the FiM state (AFM19) and the fully polarized state (FM) is very high [91.7 meV/(f.u. of $Mn_{40}In_{12}$ unit cell)]. Similarly, the AFM state without any residual moment differs largely from the FiM state [195.2 meV/f.u. of $Mn_{40}In_{12}$ unit cell)]. This discards other possible scenarios of spin configurations.

We have plotted the bandwidths for both FM and AFM19 (energetically lowest FiM state) configurations along with the Fermi surfaces corresponding to each band in Fig. 11. The width of the majority-spin channel bands are almost an order of magnitude smaller than that of the minority-spin bands, which implies a very small contribution of the DOS from the majority-spin channel at E_F. In addition, far more minority bands are contributing at E_F as compared with the majority-spin channel. The bands from both spin channels form very complicated nesting at the Fermi surfaces, as shown in the insets of Fig. 11. Fermi surfaces from majority-spin channel are mostly centered around the Γ and X points in the BZ, whereas the minority-spin channel Fermi surfaces span over the entire BZ in a more complex structure. In minority-spin channels, the hybridization among the bands crossing E_F makes the Fermi surfaces much more complex than those of the majority-spin channel. This complex nature of the Fermi surfaces makes the movement of electrons in the BZ rather unusual, which gets reflected in the quasi-half-metallic nature of the electronic structure.

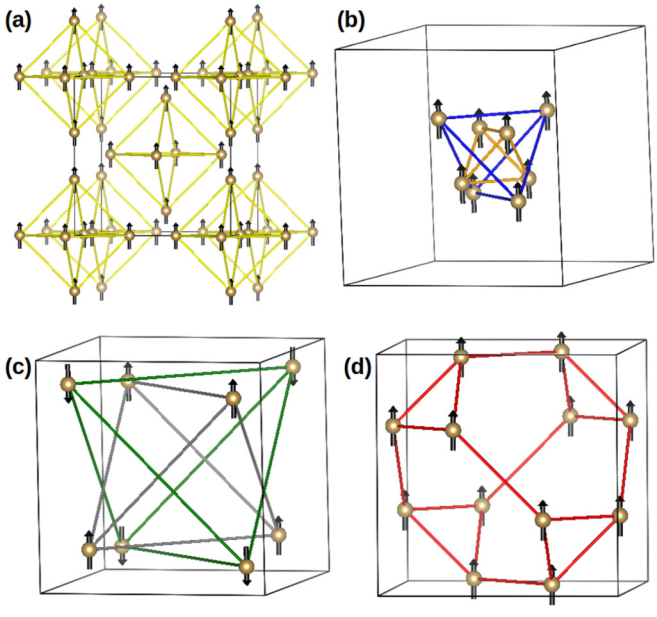

FIG. 10. The pictorial representation of the lowest energy spin configurations (i.e., AFM19) of $Mn_{40}In_{12}$: (a) octahedral units, (b) two inner tetrahedra with small (orange) and big (blue) bonds, (c) two outer tetrahedral units with small (gray) and big (green) bonds, and (d) cubo-octahedron (red bond).

V. DISCUSSION

Previous neutron-diffraction experiments [11] on Mn_3In indicate the occurrence of magnetic superlattice reflection below T_C, and the magnetic state is described as either AFM or FiM. The structure is found to be collinear with single propagation vector. A recent magnetic study [12] as well as our investigation indicate that the isothermal

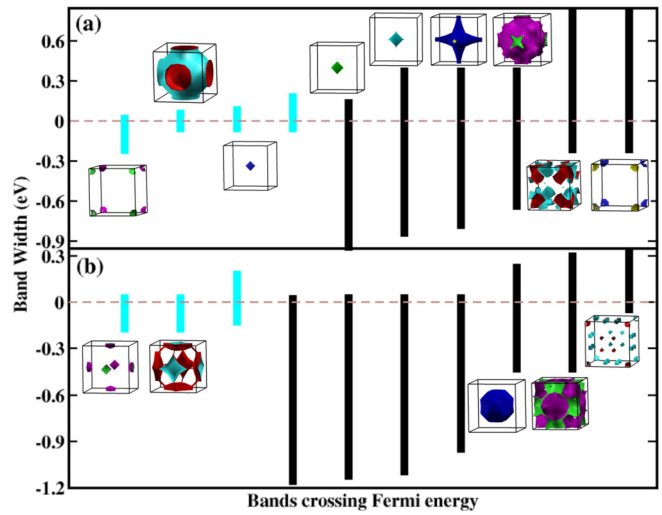

FIG. 11. The bandwidths for (a) FM and (b) AFM19 are indicated by the cyan bars (majority-spin channel) and black bars (minority-spin channel) respectively, which cross the Fermi energy. The corresponding Fermi surfaces are shown in the insets.

magnetization curve has finite coercivity, and they show an S-like feature with a small value of M at the highest field. Such observations clearly rule out a pure AFM state (without any spontaneous M), and the system is likely to have a FiM ground state. The theoretical calculations also indicate that the lowest-energy configuration (AFM19 in Table III) is FiM type with a magnetic moment of approximately $10.03\mu_B$/f.u. Here one f.u. stands for $Mn_{40}In_{12}$. In the experimental data, we do not see the full saturation of M even at 150 kOe of field. However, the value of M obtained from the 5 K isotherm at $H = 150$ kOe is found to be $14.8\mu_B$/f.u. This is reasonably close to the value obtained from the theoretical calculation.

We observe both FC and ZFC memory in the compound as well as stretched exponential type magnetic relaxation, indicating the nonergodic magnetic character typical of a SG-like state. Zhang *et al.* [12] also found a SG-like state below 45 K in their sample, although no firm evidence was provided in favor of the glassy state. On the other hand, the superlattice magnetic reflections observed in the previous neutron-diffraction experiment [11] along with our DFT calculation indicate a predominant FiM state in the system. The most likely scenario is that a SG state coexists with the long-range ordered FiM state. Similar coexistence of a long-range ordered state with a glassy magnetic state was addressed experimentally and theoretically in the past [60–64]. The coexistence occurs through the random freezing of the transverse component of the spins, while the longitudinal component shows a simultaneous long-range ordered state [60,65].

The other possible origin of the SG state is the antisite disorder caused by the secondary Mn spins occupying the In sites. For very small concentration of the Mn disorder (few ppm), the spins remain uncorrelated, while for relatively large antisite disorder (still below 10%), spins can interact with each other. The magnetic interaction in $Mn_{3+\delta}In$ is through conduction electrons by the Ruderman-Kittel-Kasuya-Yosida (RKKY) mechanism, which is long range and oscillatory in nature. The Mn atoms, sitting at the In sites irregularly, can give rise to random FM or AFM interactions as the sign of the RKKY interaction critically depends on the distance between the magnetic atoms. This can lead to spin frustration and, in presence of disorder, lead to a glassy phase.

The most important observation is the change in sign of $d\rho/dT$ close to 80 K in our $\rho(T)$ data. In general, an AFM or FiM state in the independent-electron approximation should be insulating due to the doubling of the unit cell which opens up a gap [13]. In pure metals and intermetallic compounds with a large density of free electrons, often the AFM ground state remains metallic. However, due to the superzone boundary effect associated with the AFM order, ρ shows a rise at T_C [66]. In $Mn_{3+\delta}In$, contrary to this, we find a metallic FiM state which emerges out of a PM state with $d\rho/dT < 0$ upon cooling. The electronic structure calculation of Mn_3In indicates a robust metallic state in the FiM. DFT, being a mean-field approach, does not allow us to calculate electronic states in the PM state. Therefore, it is difficult to comment on the mechanism behind the change in sign of $d\rho/dT$ from our calculations. Among transition-metal-based alloys, a similar change in the sign of $d\rho/dT$ is observed in $Fe_2TiSn_{0.75}Sb_{0.25}$, which also shows VRH type conduction at higher temperatures. The high-temperature phase with $d\rho/dT$ negative is ascribed to the localization of charge carriers due to electron-phonon interaction [67]. Similar phonon assisted carrier localization can also be mooted for the present $Mn_{3+\delta}In$ at higher temperature, which leads to negative values of $d\rho/dT$.

At this point it is important to address the role of disorder towards the electronic transport properties of Mn_3In. We found a VRH type conduction mechanism between 150 and 290 K, which indicates the electron localization. Such localization can occur due to the presence of chemical disorder (random site occupancy of Mn and In) or by random magnetic impurities [41]. The Anderson localization leading to a semiconducting or insulating state takes place for material having low carrier concentration ($n < 10^{-20}$ cm^{-3}). One can see from our Hall data that the value of n_H is low at room temperature, and the system is prone to Anderson localization due to the presence of chemical and magnetic disorders [41]. The low carrier density at higher temperature may occur due to the localization effect mediated by the electron-phonon interaction.

The Hall measurement indicates that the electron is the majority carrier both in the metallic and semiconducting phases. This is also supported by the present electronic structure calculations. On the other hand, thermopower changes sign slightly above 100 K. Below 100 K, S turns positive, indicating that holes are the majority carriers at low temperatures. This shows an apparent conflict between our Hall and thermopower data. However, the simple model (1) may not be good enough to ascertain the nature of the charge carrier from S in such a complex system. Positive thermopower is observed in pure metals such as Li, Cu, Au, and Ag, which are known to be good metals with electrons being the charge carriers. Such an anomaly is generally attributed to the complex electronic band structure near the Fermi surface [68,69].

The magnetic and transport data of the present investigation largely match well with the previous report on Mn_3In [12]. However, there are minute discrepancies between two different studies. As already mentioned, Mn_3In is prone to antisite disorder, and the degree of disorder may influence the physical properties. It is difficult to compare the antisite disorder of the present sample with the previously reported one, as x-ray refinements were not performed in the latter case. Nevertheless, we find that the absolute value of ρ is higher (both at 4 and 300 K) in the previously reported sample compared with the present one. This may indicate that the present sample has a lower value of disorder. This also corroborates well with the fact that the state with $d\rho/dT > 0$ emerges at a higher T in the present sample (75 K) than in the previous work (45 K). The disorder would tend to localize the carriers and hinder the development of a state with $d\rho/dT > 0$.

Electronic structure calculations and Fermi surfaces show that major contribution at E_F comes from the minority-spin channel DOS, while the majority-spin channel shows negligible DOS at the Fermi level. As evident from our theoretical calculation, this feature of the DOS found is extremely robust with respect to the introduction of disorder in the system. The nature of the electronic structure is found to remain unaltered in both ordered ($Mn_{40}In_{12}$ and $Mn_{36}In_{16}$) and disordered ($Mn_{40}In_{12}$ with antisite disorder) structures.

The theoretical moment from the one $Mn_{40}In_{12}$ cluster is about 10 μ_B/f.u., which indicates an effective moment per

Mn atom to be $\approx 0.25\mu_B$. In the case of recently reported fully compensated HM ferrimagnet $Mn_{1.5}FeV_{0.5}Al$ [70], the effective moment obtained experimentally at 2 K under 50 kOe of applied field is $0.026\mu_B$/Mn as compared with the value of $0.066\mu_B$/Mn for the present Mn_3In in a similar condition. This indicates that spin compensation in Mn_3In is on par with a typical compensated FiM system.

In conclusion, our DFT total-energy calculation indicates that, energetically, a FiM-type spin arrangements is the most favorable in $Mn_{3+\delta}In$. Experimentally, the system shows a glassy magnetic component along with the partly compensated FiM phase. Our investigation rules out the possibility of a fully compensated half-metallic ferrimagnetic state in this compound as previously predicted [6,7].

ACKNOWLEDGMENTS

S.C., P.D., and S.S. would like to acknowledge University Grants Commission (India), Science and Engineering Research Board (Grant No. PDF/2017/001061), and IIT Goa for their research support, respectively. S.K. thanks Department of Science and Technology, Govt. of India for providing an INSPIRE faculty research grant [Grant No. DST/INSPIRE/04/2016/000431; IFA16-MS91]. UGC-DAE-CSR, Indore, and Kolkata Centers are duly acknowledged for various low-temperature measurements. We thank Prof. Prabhat Mandal, SINP, Kolkata for the magnetic measurements.

The work of V.G. was carried out while in service.

[1] E. Faran and D. Shilo, Exp. Tech. **40**, 1005 (2016).
[2] S. Picozzi, A. Continenza, and A. J. Freeman, Phys. Rev. B **70**, 235205 (2004).
[3] I. Galanakis and P. H. Dederichs, *Half Metallic Alloys Fundamentals and Application* (Springer, Berlin, Heidelberg, 2005).
[4] I. Galanakis, P. H. Dederichs, and N. Papanikolaou, Phys. Rev. B **66**, 174429 (2002).
[5] H. van Leuken and R. A. de Groot, Phys. Rev. Lett. **74**, 1171 (1995).
[6] G. Y. Gao and K. L. Yao, Appl. Phys. Lett. **103**, 232409 (2013).
[7] S. Wurmehl, H. C. Kandpal, G. H. Fecher, and C. Felser, J. Phys.: Condens. Matter **18**, 6171 (2006).
[8] U. Mizutani, M. Inukai, H. Sato, and E. Zijlstra, in *Physical Metallurgy*, 5th ed., edited by D. E. Laughlin and K. Hono (Elsevier, Oxford, 2014), pp. 121–125.
[9] U. Mizutani, R. Asahi, H. Sato, T. Noritake, and T. Takeuchi, J. Phys.: Condens. Matter **20**, 275228 (2008).
[10] T. Noritake, M. Aoki, S.-Towata, T. Takeuchi, and U. Mizutani, Acta Crystallogr., Sect. B: Struct. Sci. **B63**, 726 (2007).
[11] J. D. Browne, N. J. Hance, G. B. Johnston, and C. F. Sampson, Phys. Status Solidi A **49**, K177 (1978).
[12] Q. Zhang, D. Li, W. B. Cui, J. Li, and Z. D. Zhang, J. Appl. Phys. **106**, 113915 (2009).
[13] N. F. Mott and Z. Zinamon, Rep. Prog. Phys. **33**, 881 (1970).
[14] http://maud.radiographema.eu.
[15] G. Kresse and J. Hafner, Phys. Rev. B **47**, 558(R) (1993); G. Kresse and J. Furthmuller, *ibid.* **54**, 11169 (1996).
[16] J. Sannigrahi, J. Sichelschmidt, B. Koo, A. Banerjee, S. Majumdar, and S. Kanungo, J. Phys.: Condens. Matter **31**, 245802 (2019).
[17] J. P. Perdew, K. Burke, and M. Ernzerhof, Phys. Rev. Lett. **77**, 3865 (1996).
[18] V. I. Anisimov, I. V. Solovyev, M. A. Korotin, M. T. Czyzyk, and G. A. Sawatzky, Phys. Rev. B **48**, 16929 (1993).
[19] S. L. Dudarev, G. A. Botton, S. Y. Savrasov, C. J. Humphreys, and A. P. Sutton, Phys. Rev. B **57**, 1505 (1998).
[20] J. K. Brandon, H. S. Kim, and W. B. Pearson, Acta Crystallogr., Sect. B: Struct. Crystallogr. Cryst. Chem. **35**, 1937 (1979).
[21] J. A. De Toro, S. S. Lee, D. Salazar, J. L. Cheong, P. S. Normile, P. Muniz, J. M. Riveiro, M. Hillenkamp, F. Tournus, A. Tamion, and P. Nordblad, Appl. Phys. Lett. **102**, 183104 (2013).
[22] P. Svedlindh, P. Granberg, P. Nordblad, L. Lundgren, and H. S. Chen, Phys. Rev. B **35**, 268 (1987).
[23] T. Chakrabarty, A. V. Mahajan, and S. Kundu, J. Phys.: Condens. Matter **26**, 405601 (2014).
[24] J. C. Phillips, Rep. Prog. Phys. **59**, 1133 (1996).
[25] J. A. Mydosh, *Spin Glasses: An Experimental Introduction* (Taylor & Francis, London, 1993).
[26] J. Kroder, K. Manna, D. Kriegner, A. S. Sukhanov, E. Liu, H. Borrmann, A. Hoser, J. Gooth, W. Schnelle, D. S. Inosov, G. H. Fecher, and C. Felser, Phys. Rev. B **99**, 174410 (2019).
[27] R. V. Chamberlin, G. Mozurkewich, and R. Orbach, Phys. Rev. Lett. **52**, 867 (1984).
[28] D. Chu, G. G. Kenning, and R. Orbach, Phys. Rev. Lett. **72**, 3270 (1994).
[29] N. Khan, P. Mandal, and D. Prabhakaran, Phys. Rev. B **90**, 024421 (2014).
[30] Y. Sun, M. B. Salamon, K. Garnier, and R. S. Averback, Phys. Rev. Lett. **91**, 167206 (2003).
[31] K. Jonason, E. Vincent, J. Hammann, J. P. Bouchaud, and P. Nordblad, Phys. Rev. Lett. **81**, 3243 (1998).
[32] S. Chakraverty, M. Bandyopadhyay, S. Chatterjee, S. Dattagupta, A. Frydman, S. Sengupta, and P. A. Sreeram, Phys. Rev. B **71**, 054401 (2005).
[33] M. Bandyopadhyay and S. Dattagupta, Phys. Rev. B **74**, 214410 (2006).
[34] P. E. Jönsson, H. Yoshino, H. Mamiya, and H. Takayama, Phys. Rev. B **71**, 104404 (2005).
[35] R. P. Singh and C. V. Tomy, J. Phys.: Condens. Matter **20**, 235209 (2008).
[36] We have fit the high-T part (150–300 K) of the $C_p(T)$ data with a function $C_{nm}(T) = \mathcal{D}(\theta_D, T) + \sum_{i=1}^{2} \mathcal{E}(\theta_{Ei}, T) + \gamma T$, where $\mathcal{D}$ and $\mathcal{E}$ are the Debye and Einstein functions, respectively, and γT is the electronic contribution. The fitted curve is extrapolated down to 2 K and is used as the lattice part of the heat capacity. We have used $C_{\rm mag}(T) = C_p(T) - C_{nm}(T)$ to calculate the magnetic contribution.
[37] D. L. Martin, Phys. Rev. B **21**, 1902 (1980).
[38] Y. Hattori, K. Fukamichi, K. Suzuki, H. Aruga-Katori, and T. Goto, J. Phys.: Condens. Matter **7**, 4193 (1995).
[39] S. Ouardi, G. H. Fecher, C. Felser, and J. Kubler, Phys. Rev. Lett. **110**, 100401 (2013).

[40] M. Seredinaa, I. Gavrikova, D. Karpenkova, M. Zheleznya, A. Bazlova, R Chatterjee, R. Y. Umetsuc, V. Khovayloa, J. Mag. Mag. Mater. **485**, 193 (2019).
[41] N. F. Mott, Adv. Phys. **21**, 785 (1972).
[42] M. M. Parish and P. B. Littlewood, Nature (London) **426**, 162 (2003).
[43] P. A. Schroeder, B. Blumenstock, V. Heinen, W. P. Pratt Jr. and S. Steenwyk, Physica B + C (Amsterdam) **107**, 137 (1981).
[44] S. Ogawa, Physica B + C (Amsterdam) **91**, 82 (1977).
[45] B. Levy, M. Sinvani, and A. J. Greenfield, Phys. Rev. Lett. **43**, 1822 (1979).
[46] K. Kadowaki and S. B. Woods, Solid State Commun. **58**, 507 (1986).
[47] M. J. Rice, Phys. Rev. Lett. **20**, 1439 (1968).
[48] S. U. Jen, B. L. Chao, and C. C. Liu, J. Appl. Phys. **76**, 5782 (1994).
[49] X. Zhang, L. Yu, S. von Molnár, Z. Fisk, and P. Xiong, Phys. Rev. Lett. **103**, 106602 (2009).
[50] A. Regnat, A. Bauer, A. Senyshyn, M. Meven, K. Hradil, P. Jorba, K. Nemkovski, B. Pedersen, R. Georgii, S. Gottlieb-Schönmeyer, and C. Pfleiderer, Phys. Rev. Mater. **2**, 054413 (2018).
[51] I. M. Tsidilkovski, *Electron Spectrum of Gapless Semiconductors*, Springer Series in Solid-State Sciences (Springer, Berlin, New York, 1996), Vol. 116.
[52] H. Goldsmid, *Thermoelectric Refrigeration* (Temple Press Books Ltd., London, 1964).
[53] G. J. Snyder and E. S. Toberer, Nat. Mater. **7**, 105 (2008).
[54] M. Inukai, K. Soda, H. Sato, and U. Mizutani, Philos. Mag. **91**, 2543 (2011).
[55] J. S. Lim, D. Saldana-Greco, and A. M. Rappe, Phys. Rev. B **94**, 165151 (2016).
[56] E. Şaşıoğlu, I. Galanakis, C. Friedrich, and S. Blügel, Phys. Rev. B **88**, 134402 (2013).
[57] C. Franchini, R. Podloucky, J. Paier, M. Marsman, and G. Kresse, Phys. Rev. B **75**, 195128 (2007).
[58] E. Şaşıoğlu, C. Friedrich, and S. Blügel, Phys. Rev. B **83**, 121101(R) (2011).
[59] See Supplemental Material at http://link.aps.org/supplemental/10.1103/PhysRevB.102.214443 for the depiction of the density of states at different values of Coulomb correlations and varied degree of disorder as obtained from the theoretical calculations. It also provides us with the ground state energy for different spin configurations.
[60] Mare Gabay and G. Toulouse, Phys. Rev. Lett. **47**, 201 (1981).
[61] Po-zen Wong, S. von Molnar, T. T. M. Palstra, J. A. Mydosh, H. Yoshizawa, S. M. Shapiro, and A. Ito, Phys. Rev. Lett. **55**, 2043 (1985).
[62] H. Yoshizawa, S. Mitsuda, H. Aruga, and A. Ito, Phys. Rev. Lett. **59**, 2364 (1987).
[63] L. Shlyk, S. Strobel, B. Farmer, L. E. De Long, and R. Niewa, Phys. Rev. B **97**, 054426 (2018).
[64] J. Dho, W. S. Kim, and N. H. Hur, Phys. Rev. Lett. **89**, 027202 (2002).
[65] S. Chillal, M. Thede, F. J. Litterst, S. N. Gvasaliya, T. A. Shaplygina, S. G. Lushnikov, and A. Zheludev, Phys. Rev. B **87**, 220403(R) (2013).
[66] M. D. Wilding and E. W. Lee, Proc. Phys. Soc., London **85**, 955 (1965).
[67] S. Chaudhuri, P. A. Bhobe, and A. K. Nigam, J. Phys.: Condens. Matter **30**, 015703 (2018).
[68] Bin Xu and M. J. Verstraete, Phys. Rev. Lett. **112**, 196603 (2014).
[69] J. Sonntag, J. Phys.: Condens. Matter **22**, 235501 (2010).
[70] R. Stinshoff, A. K. Nayak, G. H. Fecher, B. Balke, S. Ouardi, Y. Skourski, T. Nakamura, and C. Felser, Phys. Rev. B **95**, 060410(R) (2017).